





Article

Synthesis of NiFe_2O_4 -LDH Composites with High Adsorption and Photocatalytic Activity for Methyl Orange Degradation

Cristian D. Valencia-Lopez, Mario Zafra-Calvo, María José Martín de Vidales, Verónica Blanco-Gutierrez, Evangelina Atanes-Sanchez, Noemí Merayo , Francisco Fernandez-Martinez , Antonio Nieto-Marquez and Antonio J. Dos santos-Garcia *

Department of Mechanical, Chemical and Industrial Design Engineering, ETSIDI, Universidad Politécnica de Madrid (UPM), 28012 Madrid, Spain; cd.valencia@alumnos.upm.es (C.D.V.-L.); mario.zafra.calvo@alumnos.upm.es (M.Z.-C.); mariajose.martindevidales@upm.es (M.J.M.d.V.); veronica.blanco.gutierrez@upm.es (V.B.-G.); evangelina.atanes@upm.es (E.A.-S.); nmerayoc@gmail.com (N.M.); francisco.fernandezm@upm.es (F.F.-M.); antonio.nieto@upm.es (A.N.-M.)

* Correspondence: aj.dossantos@upm.es; Tel.: +34-910-677-715

Received: 27 July 2018; Accepted: 7 September 2018; Published: 12 September 2018



Abstract: The presence of hazardous chemicals in wastewater produced by industrial activities and human metropolises is threatening the availability of safe drinking water. The development of a multifunctional material coupling adsorption and photocatalytic activity is hereby particularly promising for the removal of pollutants. We have proved the adsorption and catalytic activity of NiFe_2O_4 -layered double hydroxide (LDH) composite through the degradation of methyl orange (MO) at room temperature under visible light. This degradation is enhanced by using a set of small light-emitting diodes (LEDs) providing a uniform 405 nm UV light. The remediation process is based on a first-step rapid adsorption of MO molecules by the LDH structures followed by the photocatalytic oxidation of the pollutant by the ($\cdot\text{OH}$) radicals produced by the NiFe_2O_4 semiconductor nanoparticles (NPs). The magnetic properties of the ferrite NPs allow a facile separation of the composite from the liquid media via a simple magnet. NiFe_2O_4 -LDH composite could find wide application as a highly effective adsorbent/oxidizing catalyst operating under visible or near UV light.

Keywords: magnetic adsorbents; magnetic nanoparticles; photocatalysis; Layered Double Hydroxides; water pollution; Methyl Orange degradation

1. Introduction

One of the most important recent milestones that must be addressed is the human right to water. The growth of the global human population and the increase of industrial activities is leading to an insufficient water supply to satisfy basic human, commercial and agricultural needs. A sustainable solution is the removal of pollutants in wastewater although many chemicals, dyes, pharmaceuticals or heavy metal ions cannot be destroyed by conventional treatments. Therefore, new technologies able to degrade these complex pollutants are needed. These include advanced oxidation processes (AOPs) [1–3], adsorption methods [4–6] and photocatalytic processes [7–9].

We have shown that the calcined NiFe_2O_4 -layered double hydroxide (LDH) composite can combine adsorption and photocatalytic activity for the degradation of methyl orange MO. On one hand, LDHs are hydrotalcite-like compounds with large interlayer spaces and positively charged sheets due to the substitution of Mg^{2+} for a trivalent cation. The excess positive charges are balanced by anions in the inter-layer space (for instance CO_3^{2-} , OH^- , Cl^- , etc.). LDHs calcined at moderate

temperatures originate a mixture of metal oxides (so-called layered double oxides (LDO)) with high specific surfaces. An important feature of the LDOs is the “memory effect”; that is, can the original LDH structure be reconstructed after the adsorption of anions from aqueous solution [10–13]. On the other hand, ferrite nanoparticles (NPs) are semiconductors showing band gaps with a favorable overlap with visible light. This could find application in the photocatalytic degradation of contaminants and its magnetic properties allow a facile separation of the NiFe₂O₄-LDH composite from the liquid media via a simple magnet [8,14].

In this work we have synthesized the NiFe₂O₄-LDH composite in a two-step process: hydrothermal reaction to obtain NiFe₂O₄ NPs and coprecipitation of LDH. The calculated optical band gaps indicate that NiFe₂O₄ NPs can act as photocatalysts under visible light. The adsorption of MO molecules in the interlayer space of the LDH enhance its photo-oxidation by (\cdot OH) radicals, a process that is substantially more effective under 405 nm UV light. Summarizing, NiFe₂O₄-LDH composite could find wide application as a highly effective adsorbent/oxidizing catalyst operational under visible or near-UV light.

2. Results and Discussion

2.1. Structural and Microstructural Characterization

In order to fully characterize the structure of the compounds used during the removal process we have proceeded to perform X-ray diffraction (XRD) of the individual compounds and the composites employed before and after the degradation of MO. Figure 1a shows the XRD pattern of a typical LDH compound of general formula $[M^{2+}_{1-x}M^{3+}_x(OH)_2][CO_3^{2-}]_{x/2} \cdot nH_2O$, where Mg²⁺ and Al³⁺ are divalent and trivalent cations and CO₃²⁻ is the interlayer anion. It can be indexed with the *R*–3*m* space group (S.G.) with *a* = 3.048 Å, *c* = 22.978 Å and $\alpha, \beta = 90^\circ, \gamma = 120^\circ$ lattice parameters. It presents a high degree of preferential orientation along (003) planes due to the stacking of brucite-like layers. This layered structure collapses after calcination at 450 °C for 4 h obtaining a mixture of LDOs, as can be mainly observed by the disappearance of (00*n*) maxima. Figure 1b confirms the presence of the mixture of the corresponding Al and Mg oxides. The LDH structure can be easily regenerated when LDO is immersed in water. On the other hand, all the maxima present in the XRD pattern of the NiFe₂O₄ NPs (Figure 1c) can be indexed with a cubic inverse-spinel structure (S.G. *Fd*–3*m*).

Figure 1d shows the XRD pattern of the NiFe₂O₄-LDO composite used for the degradation process. Obviously, the maxima correspond to the sum of the XRD patterns presented in Figure 1b,c. The LDH recovers its layered structure after the adsorption/degradation process, as can be observed in Figure 1e. The (003) and (006) reflections, responsible for the stacking of brucite-like layers, also display the XRD pattern. There is no appreciable displacement between the (003) reflections before and after the decontamination process, which suggests the removal of the pollutant from the interlayer space.

Transmission electron microscopy (TEM) studies reveal a bimodal size distribution of NiFe₂O₄ NPs (see Figure 2, left). The vast majority of NiFe₂O₄ NPs have a mean particle size of 6 nm and there are also particles of 20 nm. As can be seen in the images, particles tend to form agglomerates as a consequence of the high surface energy associated with the small particle size they present. The TEM micrograph of NiFe₂O₄-LDH (Figure 2, right) demonstrates the presence of NiFe₂O₄ and LDH particles. Clearly visible is the layered structure of the LDH that avoids the agglomeration of the nickel ferrite particles.

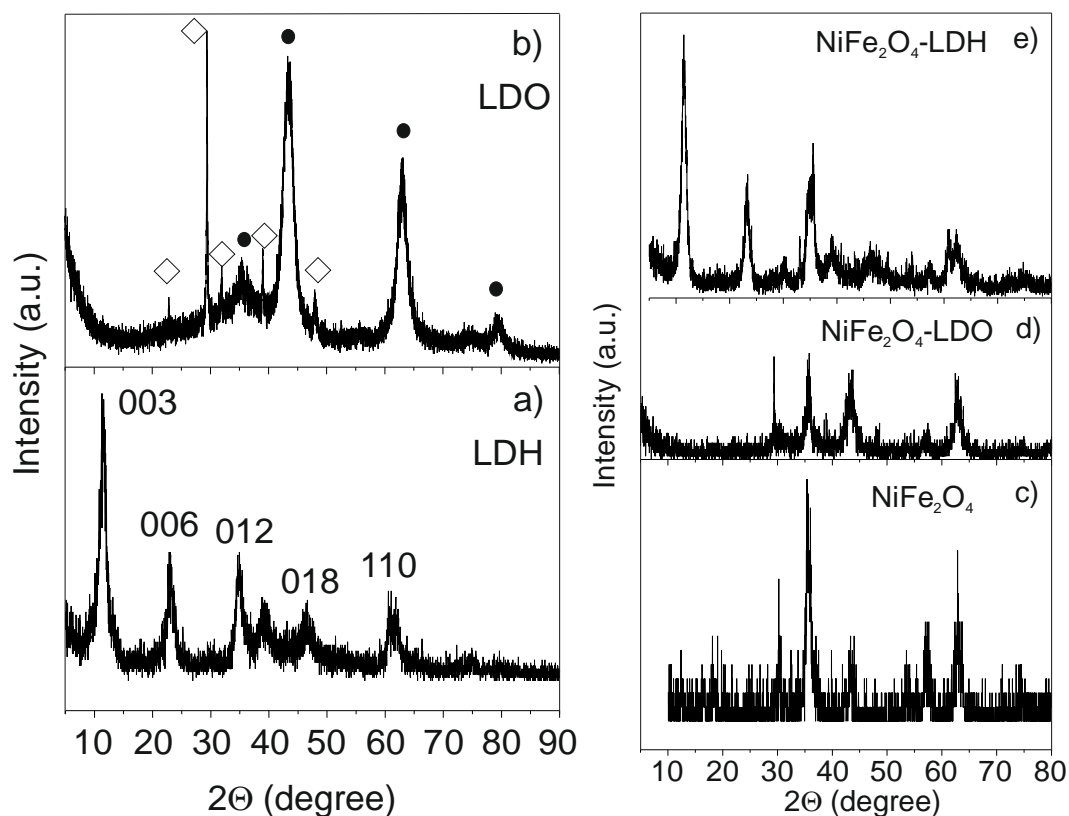


Figure 1. X-ray diffraction (XRD) patterns of: (a) as-prepared layered double hydroxide (LDH); (b) layered double oxides (LDO) mixture obtained after calcination of LDH; (c) as-prepared NiFe_2O_4 NPs; (d) NiFe_2O_4 -LDO composite before adsorption; and, (e) NiFe_2O_4 -LDH composite obtained after the methyl orange (MO) degradation.

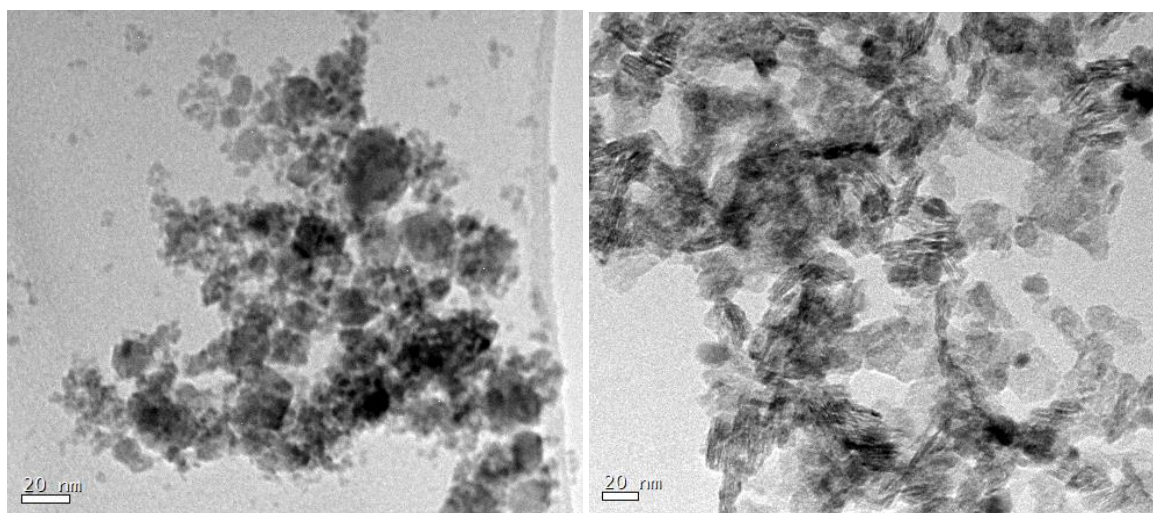


Figure 2. Transmission electron microscopy (TEM) micrograph of (left) as-prepared NiFe_2O_4 NPs and (right) NiFe_2O_4 -LDH composite.

2.2. Magnetic Properties

ZFC (zero-field-cooling) and FC (field-cooling) magnetic susceptibility measured up to room temperature (RT) is depicted in Figure 3a for NiFe_2O_4 NPs and the NiFe_2O_4 -LDH composite. A lower magnetic response is observed for the composite since the ferrite, responsible for the magnetic behavior,

is in a lower proportion. The blocking temperature (T_B) is estimated from the ZFC maximum and takes a value of 60 K for nickel ferrite particles, which agrees with other studied systems of the same composition and particle size [15]. A T_B value of 100 K is observed instead, for the composite. It is well known that for a measuring time of 100 s, the blocking temperature can be described as [16]:

$$T_B = U/25 \cdot K_B \quad (1)$$

where K_B is the Boltzmann constant and U the anisotropy barrier (KV) where K is the anisotropy constant and V the magnetic volume that may correspond to that composed of several particles if the system presents important interparticle interactions. A superparamagnetic response is obtained above the blocking temperature. Then, the particle moment is able to freely rotate. For an applied magnetic field, the anisotropy barrier that the thermal energy must overcome to obtain the superparamagnetic behavior is modified as follows [16,17]:

$$U = KV(1 - H/H_K)^2 \quad (2)$$

where H_K is the anisotropy field that indicates the intrinsic magnetic hardness of the material. Equation (2) indicates that the magnetically harder the material, the less modification of the anisotropy barrier (KV) is obtained when a magnetic field is applied. Nickel ferrite system is a soft magnetic material characterized by intense interactions between dipoles of different particles, decreasing the anisotropy constant and anisotropy field [15]. In the case of the magnetic composite, one can assume long separation distances among ferrite particles, which would avoid the dipolar interactions. Therefore, the expected larger K and H_K values would account for the larger T_B value (see Equations (1) and (2)) in the case of the magnetic composite. On the other hand, the observed irreversibility between ZFC and FC curves across all of the studied temperature range, in the case of the nickel ferrite particles, may indicate a wide blocking temperature distribution. Dipolar interactions dependent on the temperature [18] result in a magnetic volume distribution that accounts for the observed irreversibility; that is, larger magnetic volumes present larger blocking temperature values. In addition, the irreversibility temperature is close to the blocking temperature in the case of the magnetic composite. The absence of dipolar interactions in this system, as indicated before, would lead to a narrow blocking temperature distribution corresponding to a narrow magnetic volume distribution.

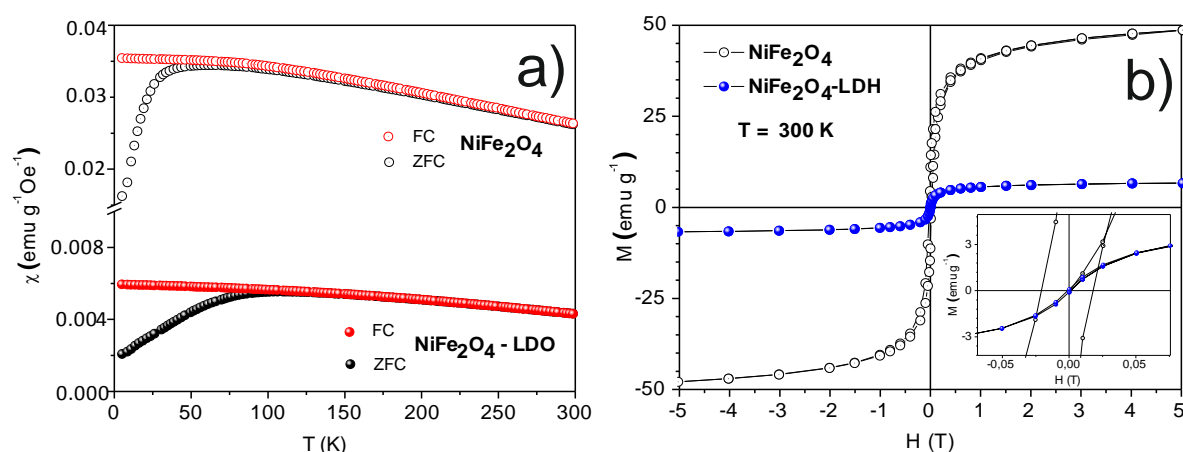


Figure 3. (a) Temperature dependent magnetic susceptibility of NiFe_2O_4 NPs and NiFe_2O_4 -LDH composite. (b) Hysteresis loops for NiFe_2O_4 NPs and NiFe_2O_4 -LDH composite at room temperature (RT). Inset shows an enlargement of the main figure.

$M(H)$ curves measured at 300 K are depicted for both samples in Figure 3b. A lower magnetic response is observed in the case of the composite since the sample presents a lower ferrite proportion.

The inset of Figure 3b illustrates an enlargement of the hysteresis loops. An almost zero coercive field for the composite can be observed, while the sample composed of NiFe_2O_4 NPs presented a coercive field close to 240 Oe, in agreement with the observed irreversibility between the ZFC and FC curves for this sample at 300 K. It is worth indicating that the absence of dipolar interactions in the case of the NiFe_2O_4 -LDH composite leads to a magnetic behavior closer to that of the superparamagnetic behavior than that of the system composed of NiFe_2O_4 NPs. The observed magnetization and coercive field values fully justify that both the nickel ferrite particles and composite systems can be removed from the liquid medium employing a simple magnet.

2.3. Thermal Stability

Figure 4 presents the temperature dependent Differential Thermal Analysis (DTA)/Thermogravimetric Analysis (TGA) curves for the NiFe_2O_4 NPs, NiFe_2O_4 -LDH-before and NiFe_2O_4 -LDH-after decontamination process. The ferrite sample presents a total weight loss of 7.6%, which contrasts to that observed in NiFe_2O_4 -LDH composites showing much higher values of weight loss (43% and 40% for NiFe_2O_4 -LDH-before and NiFe_2O_4 -LDH-after, respectively). Both NiFe_2O_4 -LDH samples show a similar thermogravimetric behavior, presenting two main weight events. The first endothermic event (the associated heat flow effects were taken using the criteria of exothermic events), from room temperature to 500 K, could be attributed to the removal of crystallization water and its physical adsorption, both on the surface and in the interlayer space. The second event in both samples is also endothermic, and occurs between 500 K and 800 K, which is attributed to the decomposition of carbonates and hydroxides, as previously reported by Deng et al. [19]. The maximum decomposition rate in this event, according to the heat signal, occurs at 660 K and 700 K for NiFe_2O_4 -LDH-before and NiFe_2O_4 -LDH-after, respectively. This can be associated with the bigger particle size of the calcined NiFe_2O_4 -LDH used for the adsorption/photodegradation process. In bigger particles, the available surface for a gas-solid reaction is lower, so the boundary layer is thicker, conducting to slower kinetics.

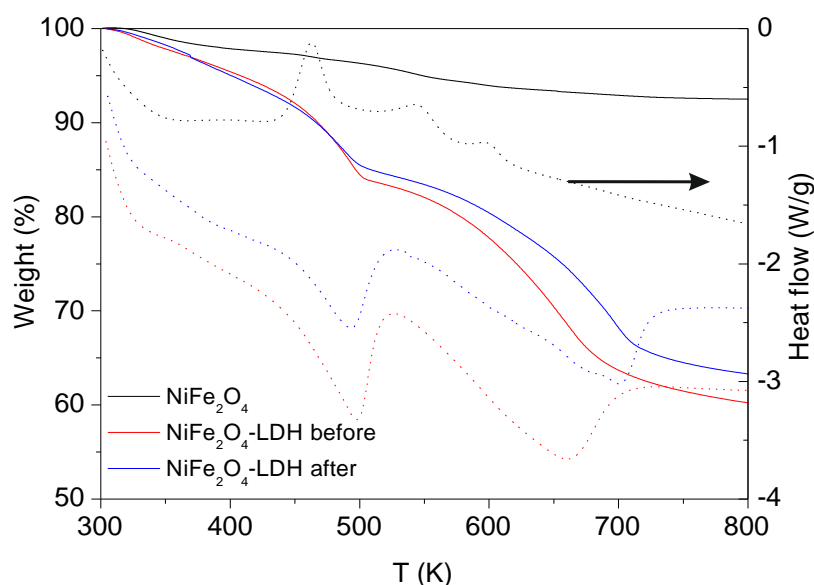


Figure 4. DTA/TGA (Differential Thermal Analysis/Thermogravimetric Analysis) of NiFe_2O_4 NPs and NiFe_2O_4 -LDH composite after and before decontamination process.

2.4. Adsorption and Photocatalytic Properties

Methyl orange degradation was tested by UV/VIS spectroscopy. Absorbance of the treated solutions was measured in an UVIKON 943 Double Beam UV/VIS Spectrophotometer from 190 to 900 nm. Approx. 0.1 g of the calcined NiFe_2O_4 -LDH composite was added to 20 mL of an aqueous

solution of 10 ppm MO under vigorous stirring for reaction times ranging from 30 to 180 min under the action of visible light. There is a clear change in the spectrum (Figure 5a) since the absorbance vanishes when the time increases. Similar results were obtained by Deng et al. for the degradation of MO by CoFe_2O_4 -LDH composite [19]. When the experiments are conducted under a 405 nm UV light (Figure 5b) the dye is eliminated more quickly through a process that is typical of most semiconductor photooxidation catalysts. The reaction continues over 150 min resulting in further oxidation ending in a colorless solution. Table 1 shows the results obtained for the removal percentage of MO.

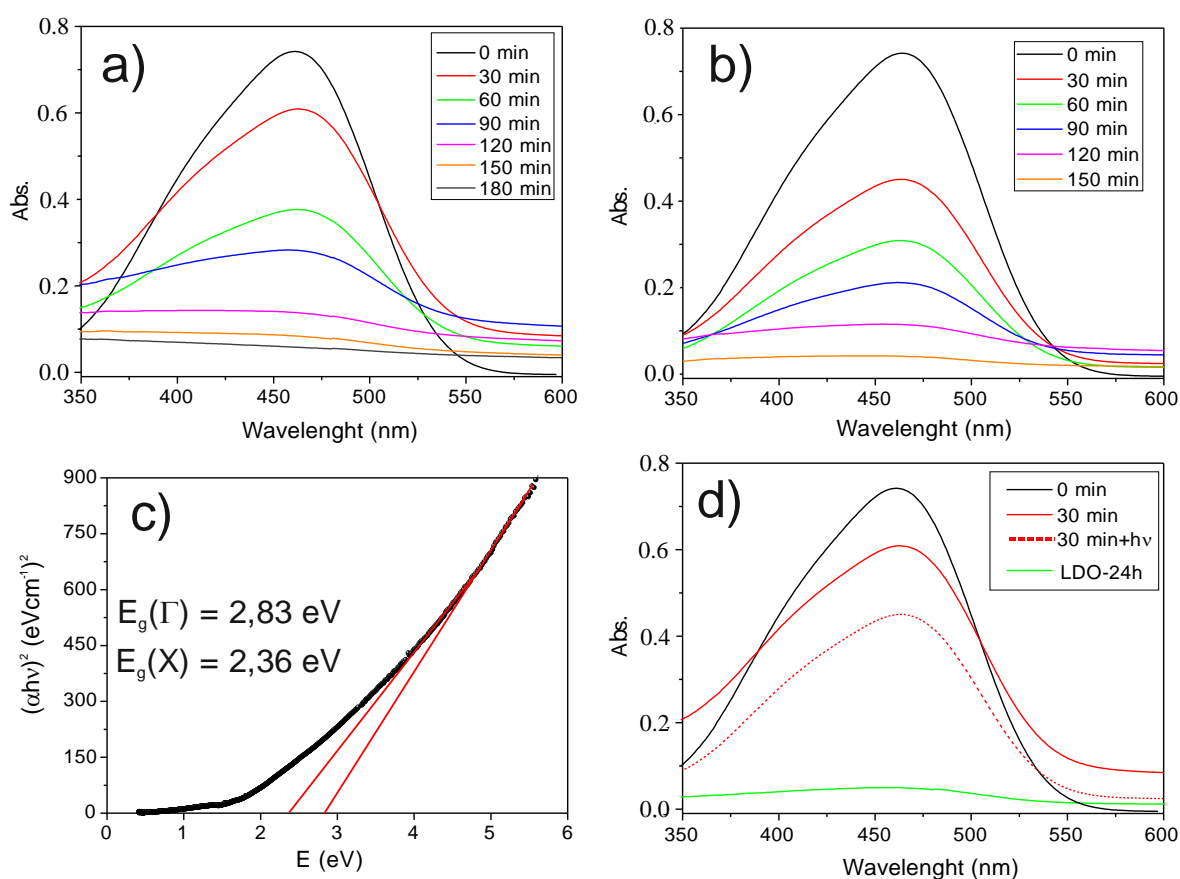


Figure 5. (a) MO in the solution after oxidation by calcined NiFe_2O_4 -LDH composite with visible irradiation and (b) with UV-405 nm irradiation. (c) Tauc plot of NiFe_2O_4 NPs showing the two direct optical band gaps. (d) Comparison of MO in the solution after 30 min of oxidation by calcined NiFe_2O_4 -LDH composite under visible and 405 nm light. Green plot shows the MO in solution after 24 h adsorption by calcined LDH.

Table 1. Removal percentage of MO at different time reactions using calcined NiFe_2O_4 -LDH composite under visible light and UV light of 405 nm.

Time (min)	% Removal (Visible Light)	% Removal (405 nm)
0	0	0
30	18.0	39.3
60	49.3	58.4
90	61.9	71.5
120	80.7	84.5
150	87.1	94.3
180	89.6	-

Concentration of MO at each reaction time was obtained from the maximum in absorbance at 464 nm.

These results point to an increase of the removal efficiency when the solution is illuminated with a near-UV light. Although MO is considered to be very stable with respect to light and difficult to oxidize, we have also performed experiments without catalyst on an MO solution illuminated with visible light and a UV light of 405 nm. The results clearly show that there is no change in absorbance at any time.

To further understand the photocatalytic process, we have calculated the energy band gap of the NiFe_2O_4 NPs by obtaining their UV–visible absorption spectrum and using the Tauc relation (Equation (3)):

$$\alpha h\nu = A(h\nu - E_g)^n \quad (3)$$

where $h\nu$ is the photon energy, h is Planck's constant, α is the absorption coefficient, E_g is the optical band gap, A is a constant (band tailing parameter) and $n = \frac{1}{2}$ for direct transitions from the valence band (VB) to the conduction band (CB). The plotting of $(\alpha h\nu)^2$ versus the photon energy ($E = h\nu$) gives a straight line in a certain region and the extrapolation of this straight line will intercept the $(h\nu)$ -axis to give the value of the direct optical energy gap (E_g). Figure 5c shows the Tauc plot for NiFe_2O_4 NPs. From the linear fit in different regions one can obtain two direct band gaps around 2.36 eV and 2.83 eV, which are in good agreement with those obtained experimentally from spatially resolved high-resolution electron energy loss spectroscopy [20].

Since the energy of the incident photons is higher than the band gap (the majority of the transitions are $\Gamma \rightarrow \Gamma$ so we have considered $E_g = 2.83$ eV), these are absorbed by the NiFe_2O_4 NPs and an electron (e^-) from the VB is promoted to the CB generating a hole (h^+) in the VB. There is a certain amount of e^- and h^+ that can recombine releasing energy as heat but some can react with adsorbed molecules on the surface of the ferrite. In aqueous solution, water molecules can transfer electrons to positive holes producing ($\cdot\text{OH}$) radicals, which are powerful oxidants. Then, the MO molecules adsorbed in the surface and in the LDH interlayer region are oxidized by ($\cdot\text{OH}$) radicals leading to the mineralization of MO to CO_2 and H_2O . The further degradation of MO into the LDH produces a displacement of the adsorption equilibrium, increasing the removal efficiency when the solution is illuminated with a near-UV light. Figure 5d shows a comparison between the spectra of the pristine MO solution and treated solutions with calcined NiFe_2O_4 -LDH composites under visible and UV light for 30 min. The degradation rate is doubled by using the UV light. The adsorption of MO by LDH particles was also evaluated with a total removal of MO after more than 24 h of treatment.

However, the main drawback of using the decolorization of organic dyes as a probe system to test photocatalyst is its tendency to undergo redox reactions with a gradual decomposition of the organic molecule [21,22]. Therefore, an evaluation of the mineralization by total organic carbon (TOC) analysis must be performed to test the total degradation of the by-products. The TOC was obtained by mathematical subtraction of the inorganic carbon (IC) content from the total carbon (TC) content [23]. The TOC determined from 10 ppm MO solution amounts to 4.42 ppm and the TOC observed after the degradation using calcined NiFe_2O_4 -LDH composite under UV light of 405 nm for 150 min amounts to 0.75 ppm. This value is close to the total conversion of the organic matter, which demonstrates the true photocatalytic disappearance of MO.

3. Materials and Methods

3.1. Synthesis of NiFe_2O_4 Nanoparticles and NiFe_2O_4 -LDO Composites

NiFe_2O_4 NPs were prepared by hydrothermal synthesis. Stoichiometric amounts of $\text{Ni}(\text{NO}_3)_2 \cdot 6\text{H}_2\text{O}$ and $\text{Fe}(\text{NO}_3)_3 \cdot 9\text{H}_2\text{O}$ nitrates (extra pure, Scharlab, Barcelona, Spain) were separately dissolved in distilled water and then mixed. The corresponding metal hydroxides were precipitated by dropping ammonium hydroxide into this solution until the pH was equal to 10. The brownish gels were filtered and sealed into a Teflon-lined stainless-steel autoclave and treated in an oven at 453 K for 12 h. The resulting powders were washed with deionized water and ethanol and then dried for 12 h at 423 K.

NiFe₂O₄-LDO composites were prepared as follows in a way similar to that described by Deng et al. [19]. Firstly, ~1 g of the as-prepared NiFe₂O₄ nanoparticles was ultrasonically dispersed into 150 mL doubly distilled water for 30 min and then heated in a water bath at 60 °C under vigorous stirring. Secondly, 12.82 g Mg(NO₃)₃·6H₂O and 9.38 g Al(NO₃)₃·9H₂O (PRS, Panreac, Barcelona, Spain) was dissolved in 100 mL of distilled water and added dropwise into the NiFe₂O₄ NPs suspension. The corresponding LDH was precipitated by adding 100 mL of an alkaline solution containing 6.75 g NaOH and 5.30 g Na₂CO₃ (extra pure, Scharlab, Barcelona, Spain). The formed suspension was aged for 8 h at 333 K and then washed with doubly distilled water until pH of the supernatant was neutral. The obtained powder was dried overnight at 333 K to obtain the NiFe₂O₄-LDH composite. Finally, the NiFe₂O₄-LDO composite was obtained through the calcination of the NiFe₂O₄-LDH composite at 723 K for 4 h.

To study the structure and the thermal stability of the LDH compound, a sample was separately prepared and then calcined at the at 723 K for 4 h to obtain the LDO mixture.

3.2. Characterizations

The samples were characterized by X-ray powder diffraction with a D5000 diffractometer (Siemens/Bruker, Karlsruhe, Germany) using Cu K $\alpha_{1,2}$ radiation operating under 30 mA and 40 kV. The diffraction profiles were collected in the range $2\theta = 5\text{--}90^\circ$ with a step-width of 0.017° .

The magnetic susceptibility was measured over the temperature range 2–300 K, using a superconducting quantum interference device (SQUID) XL-MPMS magnetometer (Quantum Design, San Diego, CA, USA) under zero-field-cooling (ZFC) and field-cooling (FC) conditions, using a DC magnetic field of 500 Oe. Magnetization measurements as a function of the applied magnetic field (H) were performed at 5 and 300 K at magnetic fields up to 5 T.

High-resolution transmission electron microscopy (HRTEM) was performed on a JEOL JEM 2100 (JEOL Ltd., Musashino, Akishima, Tokyo, Japan) operating at 200 kV fitted with a X-ray energy-dispersive spectrometer (XEDS) OXFORD INCA for the compositional analysis of each investigated crystal by in situ observations.

Thermogravimetric analyses were carried out in a SDT Q600 unit (TA Instruments, New Castle, DE, USA). Samples of 20–40 mg were heated from room temperature to 1273 K at $10\text{ K}\cdot\text{min}^{-1}$ in a $100\text{ cm}^3\cdot\text{min}^{-1}$ flow of air previously filtered.

The optical Band-Gaps of the NiFe₂O₄ NPs were obtained measuring the absorbance of NiFe₂O₄ NPs/KBr pellets in a Perkin-Elmer Lambda 900 UV–VIS–NIR Spectrometer from 190 to 3000 nm.

Total organic carbon (TOC) was measured by the combustion-infrared method using a multi N/C®3100 TOC/TN analyzer (Analytik Jena AG, Jena, Germany), which performed the catalytic combustion on cerium oxide at 1123 K.

4. Conclusions

NiFe₂O₄ NPs were synthesized by hydrothermal reaction and NiFe₂O₄-LDH composites by co-precipitation method. The calcined NiFe₂O₄-LDH composite catalyze the oxidation of MO under visible light. The work also shows that calcined NiFe₂O₄-LDH composite is substantially more effective in the mineralization of MO when illuminated with $\lambda = 405\text{ nm}$. This material could find application as an oxidizing catalyst at room temperature without pH control.

Author Contributions: M.J.M.d.V. and A.J.D.s.-G. conceived and designed the experiments; C.D.V.-L. and M.Z.-C. synthesized the materials and performed the photocatalytic test. V.B.-G. interpreted the magnetic measurements. N.M. was responsible for TOC measurements. E.A.-S. and F.F.-M. performed TGA and the absorbance of NiFe₂O₄ NPs/KBr pellets respectively. A.N.-M. and all the members above discussed the results. A.J.D.s.-G. wrote the paper with assistance of V.B.-G., E.A.-S. and A.N.-M.

Funding: This research was funded by the Spanish Ministerio de Ciencia e Innovación (MICINN) grant number MAT2017-84385-R.

Acknowledgments: The authors want to thank J.Romero-de Paz (UCM) for technical assistance with magnetization measurements.

Conflicts of Interest: The authors declare no conflict of interest.

References

1. Andreozzi, R.; Caprio, V.; Insola, A.; Marotta, R. Advanced oxidation processes (AOP) for water purification and recovery. *Catal. Today* **1999**, *53*, 51–59. [[CrossRef](#)]
2. Guinea, E.; Arias, C.; Cabot, P.L.; Garrido, P.L.; Rodriguez, R.M.; Centellas, F.; Brillas, E. Mineralization of salicylic acid in acidic aqueous medium by electrochemical advanced oxidation processes using platinum and boron-doped diamond as anode and cathodically generated hydrogen peroxide. *Water Res.* **2008**, *42*, 499–511. [[CrossRef](#)] [[PubMed](#)]
3. Martin de Vidales, M.J.; Sáez, C.; Cañizares, P.; Rodrigo, M.A. Metoprolol abatement from wastewaters by electrochemical oxidation with boron doped diamond anodes. *J. Chem. Technol. Biotechnol.* **2012**, *87*, 225–231. [[CrossRef](#)]
4. Reddy, D.H.K.; Yun, Y.S. Spinel ferrite magnetic adsorbents: Alternative future materials for water purification? *Coord. Chem. Rev.* **2016**, *315*, 90–111. [[CrossRef](#)]
5. Kharissova, O.V.; Rasika Dias, H.V.; Kharisov, B.I. Magnetic adsorbents based on micro- and nano-structured materials. *RSC Adv.* **2015**, *5*, 6695–6719. [[CrossRef](#)]
6. Moradi, A.; Najafi Moghadam, P.; Hasanzadeh, R.; Sillanpää, M. Chelating magnetic nanocomposite for the rapid removal of Pb(II) ions from aqueous solutions: characterization, kinetic, isotherm and thermodynamic studies. *RSC Adv.* **2017**, *7*, 433–448. [[CrossRef](#)]
7. Dvininov, E.; Joshi, U.A.; Darwent, J.R.; Claridge, J.B.; Xu, Z.; Rosseinsky, M.J. Room temperature oxidation of methyl orange and methanol over Pt-HCa₂Nb₃O₁₀ and Pt-WO₃ catalysts without light. *Chem. Commun.* **2011**, *47*, 881–883. [[CrossRef](#)] [[PubMed](#)]
8. Casbeer, E.; Sharma, V.K.; Li, X.-Z. Synthesis and photocatalytic activity of ferrites under visible light: A review. *Sep. Purif. Technol.* **2012**, *87*, 1–14. [[CrossRef](#)]
9. Martin de Vidales, M.J.; Mais, L.; Sáez, C.; Cañizares, P.; Walsh, F.C.; Rodrigo, M.A.; de Arruda Rodrigues, C.; Ponce de León, C. Photoelectrocatalytic Oxidation of Methyl Orange on a TiO₂ Nanotubular Anode Using a Flow Cell. *Chem. Eng. Technol.* **2016**, *39*, 135–141. [[CrossRef](#)]
10. Yang, Z.; Wang, F.; Zhang, C.; Zeng, G.; Tan, X.; Yu, Z.; Wang, H.; Cui, F. Utilization of LDH-based materials as potential adsorbents and photocatalysts for the decontamination of dyes wastewater: A review. *RSC Adv.* **2016**, *6*, 79415–79436. [[CrossRef](#)]
11. Gao, Z.; Sasaki, K.; Qiu, X. Structural Memory Effect of Mg–Al and Zn–Al layered Double Hydroxides in the Presence of Different Natural Humic Acids: Process and Mechanism. *Langmuir* **2018**, *34*, 5386–5395. [[CrossRef](#)] [[PubMed](#)]
12. Benício, L.P.F.; Constantino, V.R.L.; Pinto, F.G.; Vergütz, L.; Tronto, J.; Costa, L.M.D. Layered Double Hydroxides: New Technology in Phosphate Fertilizers Based on Nanostructured Materials. *ACS Sus. Chem. Eng.* **2017**, *5*, 399–409. [[CrossRef](#)]
13. Nagli, M.; Toroker, M.C. The electronic structure of two-dimensional transition metal hydroxide monolayers and heterostructures. *Solid State Ion.* **2018**, *314*, 149–155. [[CrossRef](#)]
14. Ren, B.; Huang, Y.; Han, C.; Nadagouda, M.N.; Dionysiou, D.D. Ferrites as Photocatalysts for Water Splitting and Degradation of Contaminants. In *Ferrites and Ferrates: Chemistry and Applications in Sustainable Energy and Environmental Remediation*; Sharma, V.K., Doong, R.-A., Kim, H., Varma, R.S., Dionysiou, D.D., Eds.; American Chemical Society: Washington, WA, USA, 2016; Volume 3, pp. 154–196. ISBN 9780841231870.
15. Blanco-Gutierrez, V.; Virumbrales, M.; Saez-Puche, R.; Torralvo-Fernandez, M.J. Superparamagnetic Behavior of MFe₂O₄ Nanoparticles and MFe₂O₄/SiO₂ Composites (M: Co, Ni). *J. Phys. Chem. C* **2013**, *117*, 20927–20935. [[CrossRef](#)]
16. Blanco-Gutierrez, V.; Climent-Pascual, E.; Saez-Puche, R.; Torralvo-Fernandez, M.J. Temperature dependence of superparamagnetism in CoFe₂O₄ nanoparticles and CoFe₂O₄/SiO₂ nanocomposites. *Phys. Chem. Chem. Phys.* **2016**, *18*, 9186–9193. [[CrossRef](#)] [[PubMed](#)]
17. Zheng, R.K.; Gu, H.; Xu, B.; Zhang, X.X. The origin of the non-monotonic field dependence of the blocking temperature in magnetic nanoparticles. *J. Phys. Condens. Matter* **2006**, *18*, 5905–5910. [[CrossRef](#)] [[PubMed](#)]

18. Virumbrales, M.; Saez-Puche, R.; Blanco-Gutierrez, V.; Torralvo-Fernandez, M.J. Discussion on the Interparticle Interactions in NiFe_2O_4 and ZnFe_2O_4 Nanosized Systems Based on the Matrix Effects in the Magnetic Behavior. *J. Phys. Chem. C* **2017**, *121*, 4029–4036. [[CrossRef](#)]
19. Deng, L.; Shi, Z.; Peng, X.; Zhou, S. Magnetic calcinated cobalt ferrite/magnesium aluminum hydrotalcite composite for enhanced adsorption of methyl orange. *J. Alloys Compd.* **2016**, *688*, 101–112. [[CrossRef](#)]
20. Dileep, K.; Loukya, B.; Pachauri, N.; Gupta, A.; Datta, R. Probing optical band gaps at the nanoscale in NiFe_2O_4 and CoFe_2O_4 epitaxial films by high resolution electron energy loss spectroscopy. *J. App. Phys.* **2014**, *116*, 103505. [[CrossRef](#)]
21. Hernández-Ramírez, A.; Medina-Ramírez, I. *Photocatalytic Semiconductors. Synthesis, Characterization, and Environmental Applications*, 1st ed.; Springer: Cham, Switzerland, 2015; ISBN 978-3-319-10998-5.
22. Herrmann, J.M. Photocatalysis fundamentals revisited to avoid several misconceptions. *Appl. Catal. B Environ.* **2010**, *99*, 461–468. [[CrossRef](#)]
23. Bisutti, I.; Hilke, I.; Raessler, M. Determination of total organic carbon—An overview of current methods. *Trends Anal. Chem.* **2004**, *23*, 716–726. [[CrossRef](#)]



© 2018 by the authors. Licensee MDPI, Basel, Switzerland. This article is an open access article distributed under the terms and conditions of the Creative Commons Attribution (CC BY) license (<http://creativecommons.org/licenses/by/4.0/>).